

# Estimation of spatial and time scales of collective behaviors of active matters through learning hydrodynamic equations from particle dynamics

Bappaditya Roy<sup>1,2,\*</sup> and Natsuhiko Yoshinaga<sup>3,1,2,†</sup>

<sup>1</sup>*Mathematics for Advanced Materials-OIL (MathAM-OIL), AIST, Katahira 2-1-1, Sendai 980-8577*

<sup>2</sup>*WPI-Advanced Institute for Materials Research (WPI-AIMR),  
Tohoku University, Katahira 2-1-1, Sendai 980-8577, Japan*

<sup>3</sup>*Department of Complex and Intelligent Systems, Future University Hakodate,  
Kamedanakano-cho 116-2, Hakodate 041-8655 Japan*

(Dated: November 7, 2024)

We present a data-driven framework for learning hydrodynamic equations from particle-based simulations of active matter. Our method leverages coarse-graining in both space and time to bridge microscopic particle dynamics with macroscopic continuum models. By employing spectral representations and sparse regression, we efficiently estimate partial differential equations (PDEs) that capture collective behaviors such as flocking and phase separation. This approach, validated using hydrodynamic descriptions of the Vicsek model and Active Brownian particles, demonstrates the potential of data-driven strategies to uncover the universal features of collective dynamics in active matter systems.

Keywords: Active matter; coarse-graining; Hydrodynamic equations; Phase transition; Machine Learning

## I. INTRODUCTION

Collective behavior is a phenomenon in which large groups of individual particles collectively move. It is ubiquitous for many-body interacting systems. Even when the interactions are local, collections of the local interaction result in large-scale behavior. When collective behavior occurs, microscopic details of the system become less critical as long as they do not change qualitative features of the system, such as symmetry. Then, hydrodynamic descriptions give us a universal insight into the system[1, 2]. However, the hydrodynamic equations are often hard to derive from microscopic models. This is because we need a small parameter to realize space and time separation. Even if such a small parameter is available, the computation to derive the hydrodynamic equations is complex. Therefore, the hydrodynamics equations are derived from the phenomenological approach in many systems.

For equilibrium systems, we may consider free energy expressed by collective variables. From the coarse-grained free energy, hydrodynamic equations can be derived from the gradient dynamics minimizing the free energy [3]. This approach cannot be applied to non-equilibrium systems in which a generic description of free energy is not available. Then, we have to coarse-grain a microscopic model, such as Langevin dynamics, into hydrodynamic equations expressed by partial differential equations. Derivation of hydrodynamic equations from microscopic models has been intensively studied in two major systems of active matters: Vicsek model[4–6] and active Brownian particles[7–9]. Their hydrodynamic descriptions are first proposed phenomenologi-

cally in [5, 6] and [8], respectively, based on the symmetry and minimum ways to break equilibrium conditions. Then, hydrodynamics descriptions expressed nonlinear partial differential equations (PDEs) are derived from the microscopic equation of the Vicsek model[10–12] and active Brownian particles[13]. These studies originate from the derivation of macroscopic equations of cytoskeleton from microscopic filament dynamics expressed by the Boltzmann equation[14] and nonlinear Fokker-Planck equations[15, 16]. From these studies, we can figure out the origins of phenomenological parameters in the hydrodynamic equations in terms of the parameters in the microscopic models. A typical assumption made for the derivation is to ignore higher-order correlation in the probability distribution of particle position and orientation. This is done by taking only two-body collision terms in the Boltzmann equation into account and decomposing pair distribution into the product of the one-body distribution in the Fokker-Planck equation. In this respect, the derived hydrodynamic equations are not *exact*, particularly at higher particle density, in which many-body correlations come into play[17]. Still, the derived hydrodynamic equations capture meso to macroscopic properties of the systems semi-quantitatively.

The challenge is to develop a systematic method to estimate hydrodynamic descriptions from the microscopic particle dynamics, which is applicable even away from the equilibrium systems. The recent development of machine learning is promising to apply to those problems. There are two steps for the coarse-graining. The first step is to identify macroscopic hydrodynamic variables. The second step is to derive macroscopic governing equations (typically expressed by PDEs) for those variables. In this study, we focus on the second step. For the Vicsek and active Brownian particles, density and polarity density are two essential variables because they are conserved or are the variables breaking symmetry. Nevertheless, we

\* roy.bappaditya@aist.go.jp

† yoshinaga@fun.ac.jp

will come back to this issue in Sec. IV.

## II. METHODS

### A. particle dynamics simulations

We should stress that our purpose is not to approximate the data of microscopic particle dynamics by macroscopic continuum equations. In the macroscopic description, details of microscopic dynamics are dropped, and only the *relevant* information, which we expect is universal, is extracted. Therefore, our approach is entirely different from recently well-studied problems of reduced-order descriptions[18]. In their study, the original dynamics are accurately approximated by low-dimensional descriptions to reproduce them. In this case, the estimation error can be measured by how the solutions of the reduced description deviate from the original dynamics. On the other hand, in our case, we do not know the ground truth a priori; the hydrodynamic description is convenient for understanding the mechanism of collective behaviors, not reproducing the microscopic details of the dynamics. The biggest problem is that we do not know how much microscopic information we should remove. This implies that it is important to clarify which length and time scales we should keep in the hydrodynamic description. Our study is motivated by this issue.

Estimation of PDEs from data is a recent growing area of machine learning. Despite the estimation of ordinary differential equations that have often been studied in time-series data analyses, the estimation of PDEs and space-time dynamics looks much harder. Several machine-learning techniques have been proposed recently, such as sparse identification of nonlinear dynamics (SINDy)[19, 20], Bayesian modeling for pattern formation[21]. In fact, these techniques have been successfully applied to pattern formation of block copolymers[21], the phase-field model for crack propagation[22], and active nematic hydrodynamics estimated from experimental data[23].

Here, we propose the method to estimate the hydrodynamic equations for two major models in active matter: the Vicsek model and active Brownian particles. We compare the estimated models with the known hydrodynamics equations proposed phenomenologically or derived from the microscopic models. Our approach is philosophically similar to the studies in [24, 25], in which PDEs are estimated from the data of active matter models. We focus rather on simpler problems of active matters, the Vicsek model, and active Brownian particles and make comprehensive studies of the estimation of hydrodynamic equations. The advantage of studying these models is that (approximated) hydrodynamic equations derived from the microscopic model are available. We also focus on the role of coarse-graining in space and time for the estimation results.

This study considers two microscopic models: the Vicsek model and Active Brownian particles (ABPs). In both models, the system is expressed by  $N$  particles residing in a two-dimensional square box of size  $L$  with periodic boundary conditions. Each particle has a position  $\mathbf{r}_i$  and a direction  $\theta_i$  (or a polarization vector  $\mathbf{p}_i = (\cos \theta_i, \sin \theta_i)$ ). Each particle exhibits self-propulsion in the direction of  $\mathbf{p}_i$  with its speed  $v_0$  when isolated. The Vicsek model has the alignment interaction between particles, and it is known to show global polar order, polar bands, cross-sea, and disordered phases depending on the particle number density and noise[12, 26]. The ABPs focus on the excluded volume interaction between particles, showing motility-induced phase separation (MIPS); namely, the system shows phase separation when the self-propulsion speed (or the Peclet number  $Pe$  defined below) is large[7, 27].

#### 1. Vicsek Model

We consider a modified version of the Vicsek model[28], where the dynamics of the particles ( $r_i, \theta_i$  for  $i = 1, 2, \dots, N$ ) are described as follows:

$$\dot{\mathbf{r}}_i = v_0 \mathbf{e}_{\theta_i}, \dot{\theta}_i = \kappa \sum_{i \neq j}^N F(\theta_j - \theta_i, \mathbf{r}_j - \mathbf{r}_i) + \eta \xi_i(t). \quad (1)$$

Here,  $\kappa$  controls the strength of alignment.  $\eta$  accounts for the amplitude of fluctuations or noise.  $\xi_i(t)$  represents Gaussian white noise with zero mean and unit variance acting on  $i$ th particle. The function  $F$  describes alignment interactions between particles. For simplicity, we choose  $F(\theta, r) = \frac{\sin(\theta)}{\pi R^2}$  if  $|r| < R$  where  $R = 1$  is the range of the interaction. This simple choice for  $F$  enforces polar alignment among the particles. While our model is based on this specific form, we expect our results to extend to more general forms of polar alignment.

We choose the unit of length and time in the simulations of the Vicsek model to be  $R$  and  $R^2/\kappa$ , respectively. Therefore, the unit length scale is the interaction range between two particles, and the unit of time scale is the time of local alignment. We set the parameters as  $N = 10000$ ,  $L = 70.6$ ,  $v_0 = 0.5$ , and the simulation time step to  $0.01\tau$  unless otherwise stated. The number density of the system is  $\rho_0 = 2$ . Previous studies have shown that numerical simulations of the Vicsek model exhibit a phase transition between a disordered state and an ordered state as the noise intensity  $\eta$  is varied[12]. The ordered state corresponds to the collective motion with the global polar alignment of the agents, while the disordered state corresponds to the random motion of the agents. Noise ( $\eta$ ) is a crucial parameter in the Vicsek

model as it determines the balance between randomness and the polar order. Therefore, to understand the system dynamics, we need to study the role of noise in the Vicsek model. Here, we collect particle dynamics data by varying the noise's strength  $\eta$ .

To collect rich information on various states, we obtain particle dynamics data under the alternating change of noise strength. First, we randomly select 10 values of  $\eta$  in  $[0.1, \eta_c]$  and 10 values in  $(\eta_c, 0.7]$  to capture the transition between ordered and disordered states. Here,  $\eta_c \approx 0.515$  is the noise strength at the transition. Then, we vary the noise strength in a piecewise linear way. At every  $100\tau_w$ , we choose  $\eta$  alternatively from a value above and below  $\eta_c$ . In total, we perform a simulation for  $2000\tau_w$  and collect 400 sampling points in time with  $\Delta t = 5\tau_w$ . Each point contains 5 snapshots to compute the time derivative of field data (see Sec. IID).

## 2. Active Brownian particles

The dynamics of active particles follow overdamped Langevin equations:

$$\dot{r}_i = \frac{1}{k_B T} D(F_i^{ex} + F_p) + \sqrt{2D}\xi_i^T, \dot{\theta}_i = \sqrt{2D_r}\xi_i^R. \quad (2)$$

The excluded-volume repulsive force  $F^{ex}$  is derived from the WCA potential  $V^{ex} = 4\epsilon[(\frac{R}{r})^{12} - (\frac{R}{r})^6]$  if  $r < 2^{1/6}$ .  $F_p$  is the self-propulsion force, and in the absence of interactions, particles move with speed  $v_0 = DF_p/k_B T$ . Diffusion constants follow the Stokes-Einstein relationship, and  $\xi_i^T$  and  $\xi_i^R$  are Gaussian white noise.

We make the equations dimensionless using  $R$  and  $k_B T$  as basic units of length and energy, respectively. The unit of time scale is chosen as  $\tau = R^2/D$ . This is the time scale of translational diffusion by which an isolated particle, on average, moves the distance of particle diameter. The rotational diffusion constant is  $D_r = 3D/R^2$ , and accordingly, the rotational diffusion time is  $\tau_r = \tau/3$ . We perform simulations with  $N = 40000$  active particles and periodic boundary conditions in a box of size  $L = 220$ . The simulation time step is  $10^{-5}\tau$ . The system is characterized by the packing fraction  $\rho = N\pi(R/2)^2/L^2$  and the Péclet number  $Pe = v_0 \frac{\tau}{R}$ . For the Active Brownian Particle model, the Péclet number (Pe) is the key parameter that controls the transition from a non-MIPS state to a MIPS state. By fixing the particle density at  $\rho_0 = 0.65$ , we can observe the phase transition by varying the Pe of the system[27]. The system remains in a disordered state for sufficiently small values of Pe, while for large enough values of Pe, the system exhibits MIPS. Under our choice of  $\rho_0$ , phase separation occurs at  $Pe \approx 60$ . In our study, we use data of various values of Pe, perform numerical simulations, and analyze the kinetics during the phase transition.

To include both information on the phase-separated (MIPS) and non-MIPS regimes and the transitions between them, we performed simulations with various

Peclet numbers, covering a range below the transition ( $Pe = 0, 20, 40$ ) around the transition point ( $Pe = 60$ ), and above the transition ( $Pe = 80, 100, 120$ ). The total time of each simulation is  $40.4\tau$ , and we collect 100 sampling points in time with  $\Delta t = 0.404\tau$ .

## B. Learning hydrodynamic equation

We introduce a learning framework that uses microscopic discrete particle data as input and produces sparse, interpretable, most expected hydrodynamic equations as output (see Fig. 1). We demonstrate it for the simulation data of the two models, the Vicsek model and the ABPs. In these particle models,  $N$  particles are initially randomly distributed and oriented on a domain. The discrete data sets of the particle's trajectories ( $r_i(t)$ , where  $i = 1, 2, \dots, N$ ) along with particle orientation ( $\theta_i(t)$ ) at discrete times ( $t, t + \Delta t, \dots, t + T\Delta t$ ) are collected. We then transform the discrete data into continuum fields at each snapshot. Subsequently, we can derive hydrodynamic equations for density field  $\rho(t, x)$  and polarization density field  $\mathbf{p}(t, x)$ . This process involves constructing over-complete and estimating the most likely dictionary terms encompassing all conceivable right-hand-side terms, aligning with symmetries and conservation laws. We numerically evaluate the values of these terms using the field data (see Sec. IIE). At each sampling point, we compute the spatial and time derivatives of the fields. To compute the time derivative, we use 5 snapshots at each sampling point. The dictionary terms and time derivative obtained from the data are used for the estimation of the coefficients  $\mathbf{w}$ . To realize coarse-graining in time, the time derivatives are computed at different time intervals of  $\tau_w$  (See Sec. IID). The coarse-graining in space is made by using a filter of wavenumbers when the inverse Fourier transformation of each dictionary term is performed. We will explain the details of each step in the next sections.

## C. Hydrodynamic fields

After collecting all particle trajectories and orientation data, we first transform particle positions and orientations into continuous fields, using a widely used convolution kernel approach[29]. This is the first stage of the coarse-graining process, aimed at discarding microscopic information below the particle length scale. For  $x_i$  and  $\mathbf{p}_i$  representing particle positions and orientations, respectively, the density field  $\rho(t, x)$  and polarization density field  $\mathbf{p}(t, x)$  can be obtained by

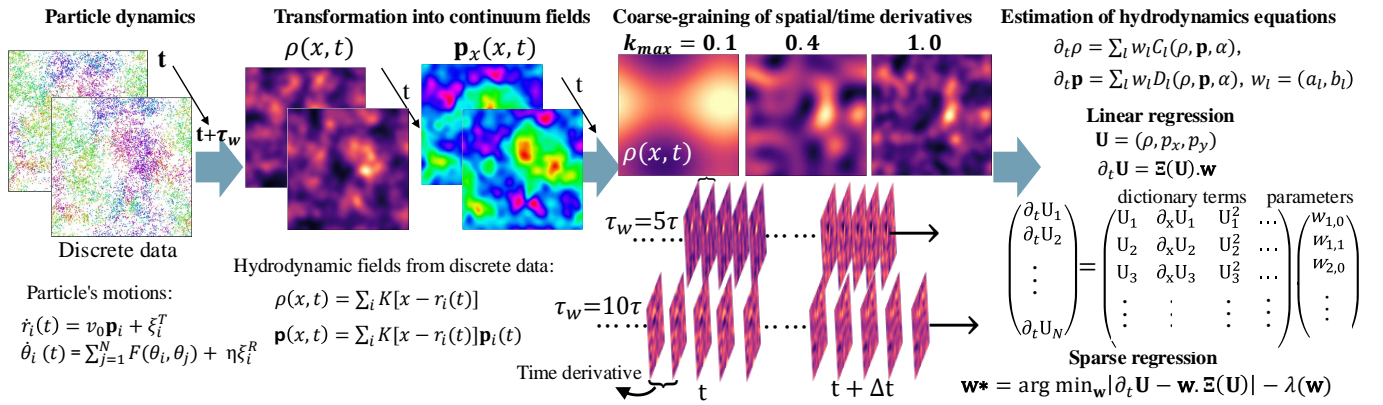


FIG. 1. (Color online) Schematic illustration of estimation of hydrodynamic equations from particle dynamics.

$$\rho(t, x) = \sum_{i=1}^N K[x - r_i(t)] \quad (3)$$

$$\mathbf{p}(t, x) = \sum_{i=1}^N K[x - r_i(t)] \mathbf{p}_i(t), \quad (4)$$

where  $K(x) = \frac{1}{2\pi\sigma^2} \exp[-|x|^2/2\sigma^2]$  is the Gaussian kernel. Here, we choose  $\sigma = 2$ , which determines the minimum spatial resolution. Coarse-graining of the system beyond the length scale of the particle size will be treated in Sec. II D.

#### D. Spatial and temporal derivatives of coarse-grained fields

A fundamental task in estimating hydrodynamic equations is the calculation of spatial and temporal derivatives of coarse-grained fields. This enables us to represent the coarse-grained fields using basis functions, such as polynomials and Fourier modes. In this context, we compute the time derivatives of the density field and polarization density field using polynomial finite differentiation at a point, considering different time windows for the time derivatives. Understanding how derivatives behave over various time scales enhances the accuracy and robustness of these models, providing a multi-scale perspective essential for effective coarse-graining. This approach allows for selecting appropriate time scales for coarse-graining, striking a balance between capturing essential dynamics and reducing computational complexity. Additionally, Fourier transformation is extensively used for the spatial derivatives on the coarse-grained field with a wave vector  $\mathbf{k} = (k_x, k_y)$ . Therefore, the spectral representation allows for efficient computation of space and time derivatives.

Coarse-graining is applied both spatially and temporally. Temporal coarse-graining is essential for computing the time derivatives of the density and polarization

fields achieved using the polynomial finite differentiation. To accommodate various time scales in the coarse-graining process, we collect the data at different intervals. We set  $\tau_w \in [0.1\tau, 50\tau]$  for the Vicsek model and from  $\tau_w \in [10^{-3}\tau, 0.5\tau]$  for ABPs. Therefore, time scales  $\tau_w$  for coarse-graining are one of the essential parameters of our methods. In the same way, we can also implement spatial coarse-graining on each time frame at fixed time scales for every individual dictionary function. Initially, we perform a Fourier transformation on all dictionary functions and the time derivative of the density and polar density functions. This brings us to the wavenumber domain of all the terms. We select various wave vector  $\mathbf{k}$  value ranges in this domain and employ filtering techniques in the dictionary function. We consider the values of  $k = |\mathbf{k}|$  ranging in  $k \in [0, k_{max}]$ . Our aim is to collect the data in the wavenumber domain only for these particular ranges of  $k$  values and discard the rest. For smaller values of  $k_{max}$ , this approach captures the dynamics from long wavelengths, removing most of the microscopic information. In contrast, for larger values of  $k_{max}$ , it captures all the information at the microscopic level with short-range wavelengths.

#### E. Estimation of hydrodynamic equations

Besides many methods for the data-driven discovery of dynamical systems, SINDy provides a promising way to identify the dynamical equations from data[20]. To discover PDEs from data, we select only the most informative terms about the dynamics, efficiently handling spatiotemporal data, a key feature of many models. We use sparse regression to estimate the hydrodynamic equations consistent with the data of coarse-grained fields discussed in the previous section. For this purpose, we first create a comprehensive set of dictionary terms that adhere to symmetries and conservation principles. We achieve this by gathering individual spatial derivative variables and other hydrodynamic quantities. Moreover, to explore the complexities of parameterized systems, the

SINDy method [19] can be extended to analyze parameterized systems by incorporating the parameter as an additional variable in the governing equations. We focus on two non-equilibrium dynamical models, the Vicsek Model and the ABPs. These models exhibit significant sensitivity to the parameters  $\eta$  and  $Pe$ , respectively. Variations in these parameters can drive the systems through phase transitions, resulting in transitions between distinct dynamical states. By systematically varying these parameters and collecting time-series data, we can comprehensively characterize the range of dynamical behaviors exhibited by both models. Here, we emphasize 26 dictionary terms, including the parameter-dependent terms related to the density field, and 22 dictionary terms for polarization fields, ensuring a focus on aspects most relevant to hydrodynamics.

We use parameterized and nonlinear hydrodynamic equations for density  $\rho(\mathbf{r}, t)$  and polarity density  $\mathbf{p}(\mathbf{r}, t)$  with possible candidate dictionary terms in the general form

$$\partial_t \rho = \sum_l a_l C_l(\rho, \mathbf{p}, \alpha) \quad (5)$$

$$\partial_t \mathbf{p} = \sum_l b_l D_l(\rho, \mathbf{p}, \alpha) \quad (6)$$

$$\dot{\alpha} = 0 \quad (7)$$

Here,  $C_l(\rho, \mathbf{p}, \alpha)$  and  $D_l(\rho, \mathbf{p}, \alpha)$  are the candidate dictionary terms and functions of the fields and their spatial derivatives (See. Eq. (A1) and Eq. (A2)). We also add a parameter controlling the phase transition into the dictionary terms, namely,  $\alpha = \eta$  for the Vicsek model and  $\alpha = Pe$  for the active Brownian particles. With this approach, we may estimate not only the dependence of  $C_l$  and  $D_l$  on the variables  $\rho$  and  $\mathbf{p}$  but also on the control parameter  $\alpha$ [19].

To estimate the PDEs of Eq. (5) and Eq. (6), we perform the following procedure. First, we construct a linear relation of  $\partial_t \mathbf{U} = \Xi(\mathbf{U}) \cdot \mathbf{w}$ , where the left-hand side is the time derivatives of the fields,  $\mathbf{U} = (\rho, p_x, p_y)$ . The coefficients  $\mathbf{w} = (a_l, b_l)$  are coefficients in the hydrodynamics equations and to be estimated. The row direction of the matrix  $\Xi(\mathbf{U})$  indicates the numerical values of the dictionary terms  $C_l(\rho, \mathbf{p}, \alpha)$  and  $D_l(\rho, \mathbf{p}, \alpha)$  obtained from data. The column direction of the matrix  $\Xi(\mathbf{U})$  indicates different sampling points in space and time. The data with different values of control parameter  $\alpha$  is stacked in the column direction. For each variable,  $\rho$ ,  $p_x$ , or  $p_y$ , the dimension of  $\Xi(\mathbf{U})$  is  $N_d \times M$ , where  $N_d$  is the total number of sampling points (including different parameter values) and  $M$  is the number of dictionary terms. We aim to infer a parsimonious model, making the vector  $\mathbf{w}$  sparse. Importantly, every nonzero value of  $\mathbf{w}$  corresponds to a term in the hydrodynamic description. Here, the sparse  $\mathbf{w}$  means only a few terms are active. Therefore, to estimate the hydrodynamics coefficients  $\mathbf{w}$ , we

use the sparse regression algorithm from SINDy[19, 20].

$$\mathbf{w}^* = \underset{\mathbf{w}}{\operatorname{argmin}} |\partial_t \mathbf{U} - \Xi(\mathbf{U}) \cdot \mathbf{w}|^2 + \lambda(\mathbf{w}), \quad (8)$$

where  $\lambda(\mathbf{w})$  is a regularization term that controls the level of sparsity. There are many ways to realize sparsity by the regularization term. In [19, 20], sequential thresholding of estimated parameters  $\mathbf{w}$  was used. In this approach, first, the ridge regression  $\lambda(\mathbf{w}) = \lambda_0 |\mathbf{w}|^2$  is used to estimate  $\mathbf{w}$ . Then, all the parameters smaller than a certain value are set to 0. By iterating the process, a few nonzero parameters are estimated.

In this work, we use a slightly different approach motivated by the method by [24]. This method involves iterating through a series of steps based on the number of dictionary terms. At each iteration step, first, we use ridge regression with the regularization parameter  $\lambda_0 = 10^{(-5+w_r)}$ , where  $w_r$  is the sum of the power of fields present in each dictionary term. Then, we eliminate one dictionary term with the smallest coefficient in its magnitude, considering it less important for particle dynamics. Concurrently, we calculate the error after each dictionary term elimination. From the way to change the error  $E(n)$  as a function of nonzero dictionary term  $n$ , we evaluate the optimal number of dictionary terms  $n^*$ . The error is derived from the sum of squared differences between the predicted values ( $\Xi(\mathbf{U})$ ) and the actual values ( $\partial_t \mathbf{U}$ ). Specifically, the error is defined as

$$E(n) = \frac{1}{N_d} \sqrt{\sum_{i=1}^{N_d} (\Xi(\mathbf{U}_i) \cdot \mathbf{w}_i(n) - \partial_t \mathbf{U}_i)^2}. \quad (9)$$

Here,  $n$  represents the iteration step (i.e., the number of remaining dictionary terms), and  $N_d$  is the total number of spatio-temporal sampling data points. Typical dependence of the error on  $n$  can be seen in Fig. 2(b). It can be observed that moving from right to left on the plot, the error  $E$  remains almost constant as each dictionary term is eliminated. However, after eliminating a certain dictionary term, the error  $E$  suddenly increases. We define  $n^*$  by the number of nonzero dictionary terms at which the error starts to deviate from its saturation value. Quantitative definition of  $n^*$  is following: By fitting  $E(n)$  using the initial five points from the right and extrapolating it, we obtain a linear regression line (shown in solid red). We construct two additional dotted lines above and below the regression line, separated by an interval of  $\delta E = 0.005$ . We define  $n^*$  when the error crosses the dotted line. Note that in [24],  $d^2 E(n)/dn^2$  was used to define  $n^*$ . This approach does not work in our system because the error decreases as a function of  $n$  in multiple steps. We will discuss this issue in Sec. V C.

### III. VICSEK MODEL

Let us start with estimation results for the Vicsek model under specific coarse-graining parameters in space

$k_{\max}$  and time  $\tau_w$ . When  $k_{\max} = 0.1$  and  $\tau_w = 40\tau$ , we obtain the hydrodynamic equations for density  $\rho(\mathbf{r}, t)$  and polarity density  $\mathbf{p}(\mathbf{r}, t)$

$$\partial_t \rho = a_1 \nabla \cdot \mathbf{p} \quad (10)$$

$$\begin{aligned} \partial_t \mathbf{p} = & b_1 \nabla \rho + b_2 (\mathbf{p} \cdot \nabla) \mathbf{p} + b_3 (\nabla \cdot \mathbf{p}) \mathbf{p} + b_4 \nabla |\mathbf{p}|^2 \\ & + \alpha(\rho, \eta) \mathbf{p} + \beta(\rho, \eta) |\mathbf{p}|^2 \mathbf{p}, \end{aligned} \quad (11)$$

where  $a_1 = -0.403$ ,  $b_1 = 0.23$ ,  $b_2 = -0.049$ ,  $b_3 = -0.047$ , and  $b_4 = 0.024$ . The coefficients for linear and cubic terms in  $\mathbf{p}$  are, respectively,  $\alpha = b_5 + b_6 \rho + b_7 \eta \rho^2$  and  $\beta = b_8 \eta$  with  $b_5 = -0.00093$ ,  $b_6 = 0.00032$ ,  $b_7 = 0.0016$ , and  $b_8 = -0.0017$ . These terms do not contain spatial derivatives, and we call them *bulk terms*. On the other hand, the terms in the first line of Eq.(11) contain first spatial derivatives. We call them *advection terms* [30].

The error in the estimation is small for the equation of density  $E \simeq 0.09306$ , whereas for the polarity density,  $E \simeq 0.3069$ . During the estimation process, the error suddenly decreases as in Fig.2(a) when the term  $\nabla \cdot \mathbf{p}$  is included in the hydrodynamic equation for the density field. Additional terms do not improve the estimation, suggesting that  $\nabla \cdot \mathbf{p}$  is the most relevant term in the density dynamics. Because the density flux is dominated by the flow of self-propelled particles in the Vicsek model, it is reasonable that the flux is proportional to  $\mathbf{p}$ . The coefficient of this term is  $a_1 \approx 0.4$  in Eq. (10), which is close to the speed of an individual particle  $v_0 = 0.5$ . On the other hand, the error in the hydrodynamic equation for the polarity density decreases in multiple steps, as shown in Fig. 2(b). The error decreases mostly by the four terms of  $\nabla \rho$ ,  $(\mathbf{p} \cdot \nabla) \mathbf{p}$ ,  $(\nabla \cdot \mathbf{p}) \mathbf{p}$ ,  $\nabla |\mathbf{p}|^2$ . Still, the error does not reach its minimum value. The additional four terms decrease the error further. Beyond 8 terms, the error saturates and does not decrease further. This additional decrease of the error is due to the bulk terms, such as  $\mathbf{p}$ ,  $\rho \mathbf{p}$ ,  $\eta \rho^2 \mathbf{p}$ ,  $\eta |\mathbf{p}|^2 \mathbf{p}$ .

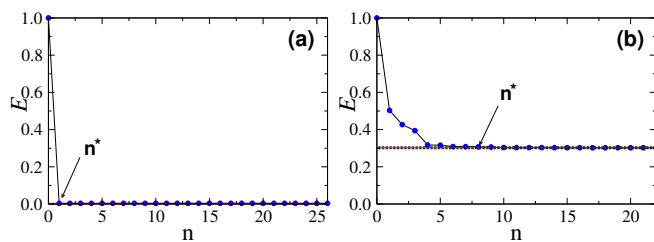


FIG. 2. (Color online) Error  $E$  vs  $n$  for density field (a) and polarity (b) in the Vicsek model. The optimal numbers of terms are estimated as  $n^* = 1$  in (a) and  $n^* = 8$  in (b) at  $\tau_w = 40\tau$  and  $k_{\max} = 0.1$ .

All the estimated terms in Eq. (11) is coincident with what was studied in the phenomenological hydrodynamic equation[5] and the hydrodynamic equation derived from the Vicsek model[10]. However, the estimated hydrodynamic equation misses several terms. First, all the diffusive terms in the polarity density, such as  $\Delta \mathbf{p}$ ,  $\nabla(\nabla \cdot \mathbf{p})$ , and  $(v \cdot \nabla)^2 \mathbf{p}$ , are not estimated. The anisotropic pressure

term  $\mathbf{p}(\mathbf{p} \cdot \nabla \rho)$  is also missing. Note that the anisotropic parts of the diffusive terms and the anisotropic pressure were not obtained by the derivation of the hydrodynamic equation from the Vicsek model[10]. The second issue is the terms that are dependent on noise. In the Toner-Tu model, the  $\mathbf{p}$  coefficient increases as the noise amplitude decreases and its sign changes. As a result, the polarity density  $\mathbf{p}$  takes a finite value, whose magnitude is determined by  $|\mathbf{p}| = \sqrt{-\alpha/\beta}$ . As we decrease the amplitude of noise,  $\eta$ , the sign of  $\alpha$  changes and, as a result, the phase transition from the disordered state  $|\mathbf{p}| = 0$  to the ordered state  $|\mathbf{p}| \neq 0$  occurs. However, in our results, the dependence of  $\eta$  on  $\alpha$  and  $\beta$  is not properly reproduced. This may be because the decrease of error is dominated by the advection terms and the bulk terms make less contribution to the error. We come back to this issue in Sec. V D. In the deviation of hydrodynamic equations from the Vicsek model, in principle, all the coefficients are dependent on the amplitude of noise[10].

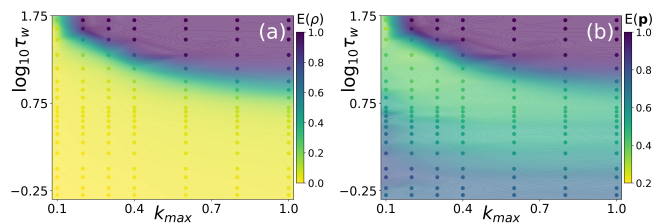


FIG. 3. (Color online) Error plot in  $(k_{\max}, \tau_w)$  space for density (a) and polarity (b) in the Vicsek model. The color bar represents the change of error.

Now, we study how the estimation results depend on coarse-graining length scale  $k_{\max}$  and time scales  $\tau_w$ . For the density field, the error is small, independent of the spatial and time scales, except for large  $\tau_w$  and  $k_{\max}$  (Fig. 3(a)). The estimated number of terms is always one. On the other hand, the error for the polarity density is strongly dependent on the spatial and time scales (Fig. 3(b)). In fact, the minimum error for the polarity density is attained at a larger length scale  $k_{\max} \approx 0.1$  and a longer time scale  $\tau_w \approx 40\tau$ . The results suggest that the hydrodynamic equations are valid only when the spatial scale is larger than  $l = 2\pi/k_{\max} \approx 30R$  and the time scale is longer than  $10\tau$ . We will compare these length and time scales with the intrinsic scales of the Vicsek model in Sec. V A.

From the results of the error in  $(k_{\max}, \tau_w)$ , shown in Fig. 3, we found that the error of the estimation is dominated by a few terms. For the hydrodynamic equation of density field, the error decreases as the coefficient of  $\nabla \cdot \mathbf{p}$  approaches  $-0.5$  (see Fig. 4(a)). In fact, the minimum error for the density field is attained at  $k_{\max} = 0.1$  and  $\tau_w = 0.5\tau$ . In this case, the estimated coefficient is  $a_1 = 0.499$  and closer to  $-0.5$  than the case of  $\tau_w = 40\tau$  shown above. Note that  $\tau_w$  at which the error of density field is minimum is different from  $\tau_w = 40\tau$  at which the error of the polar density is minimum. Still, the differ-

ence in the error of the density field between  $\tau_w = 0.5$  and  $\tau_w = 40\tau$  is small. Therefore, it is reasonable to take  $k_{\max} = 0.1$  and  $\tau_w = 40\tau$  as an optimal scale of the hydrodynamic equations.

The error of the hydrodynamic equation of polarity density decreases as the coefficient of  $\nabla\rho$  approaches  $-0.25$ . These results are consistent with those coefficients obtained from the Boltzmann equation: namely,  $-v_0$  and  $v_0/2$ , respectively [10]. Although the smallest error is attained by small  $k_{\max}$  and large  $\tau_w$ , the error at larger  $k_{\max}$  and intermediate  $\tau_w$  is also small. Both regions have the coefficient of  $\nabla\rho$  close to  $-0.25$ . The error is smallest at small  $k_{\max}$  because the bulk terms can be estimated only in this region.

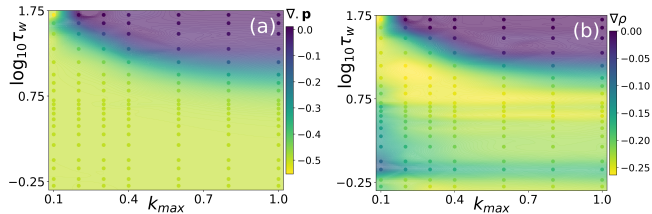


FIG. 4. (Color online) Plot of coefficients of dictionary terms  $\nabla \cdot \mathbf{p}$  (a) and  $\nabla\rho$  (b) in  $(k_{\max}, \tau_w)$  space.

The estimated coefficients are dependent on the spatial and time scales. For the hydrodynamic equation of polarity density, the four terms,  $\nabla\rho, (\mathbf{p} \cdot \nabla)\mathbf{p}$ ,  $(\nabla \cdot \mathbf{p})\mathbf{p}$ , and  $\nabla|\mathbf{p}|^2$ , are estimated for all time and length scales, as shown in Fig. 5(b). On the other hand, Fig. 5(a) shows that the bulk terms, such as  $\mathbf{p}, \rho\mathbf{p}, \rho^2\mathbf{p}, |\mathbf{p}|^2\mathbf{p}$ , are estimated only when  $k_{\max}$  is small. Because the bulk terms do not contain spatial derivatives, these terms may be comparable with the advection terms only when the wavenumber is small.

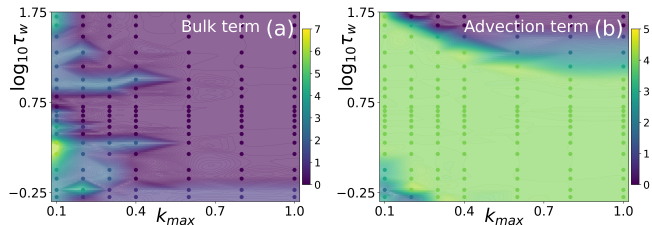


FIG. 5. (Color online) Plot of the total number of bulk terms (a) and total number of advection terms (b) in each point of the parameter  $(k_{\max}, \tau_w)$  space.

#### IV. ACTIVE BROWNIAN PARTICLES

In the case of ABPs, our estimation result is

$$\partial_t \rho = \nabla \cdot [f_1(\rho, \text{Pe})\mathbf{p}] + \Delta f_2(\rho, \text{Pe}) + \Delta^2 f_3(\rho, \text{Pe}) + \mathcal{N}[\rho, \mathbf{p}] \quad (12)$$

$$\mathbf{p} = \nabla g_1(\rho, \text{Pe}) + \nabla \Delta g_2(\rho, \text{Pe}), \quad (13)$$

when  $k_{\max} = 0.1$  and  $\tau_w = 0.02\tau$ . Equation Eq. (13) requires an explanation. First, we estimate the coefficients of the hydrodynamic equation in the form of Eq. (6). The error of this estimation is shown in Fig. 6(e). Even if we include all the dictionary terms, the error remains high,  $E \simeq 1$ . This result suggests that the polarity density  $\mathbf{p}$  is not a hydrodynamic variable. The polarity density  $\mathbf{p}$  is slaved by the density field  $\rho$ . Then, instead of Eq. (6), the polarity density should be expressed by the function of the density field. Therefore, we consider the following estimation:

$$\mathbf{p} = \sum_l \tilde{b}_l \tilde{D}_l(\rho, \alpha) \quad (14)$$

with the coefficients  $\tilde{b}_l$  for each dictionary term (see Eq.(A3)).

The error is shown in Fig. 6(c). In this case, the error decreases in two steps. First, the error decreases significantly by the term  $\text{Pe}\nabla\rho^2$ , and then it decreases slightly by the additional 5 terms. Finally, the error saturates at  $E \simeq 0.4$ . The estimated terms are shown in Eq. (13). The estimated terms,  $f_1, f_2, f_3, g_1, g_2$ , in Eq. (12) and Eq. (13) are polynomials of  $\rho$  and linear functions of  $\text{Pe}$ . The detailed expressions of the coefficients are shown in Appendix A 2.

The estimation of the density equation works similarly to the Vicsek model, suggesting that the density is a hydrodynamic variable in this model. As we increase the number of terms, the estimation error decreases in three steps, as shown in Fig. 6(a). First, the error decreases significantly by 5 terms, which are  $\Delta\rho, \Delta\rho^2, \text{Pe}\nabla \cdot \mathbf{p}, \text{Pe}\Delta\rho^2, \text{Pe}\nabla \cdot (\rho\mathbf{p})$ . Among those terms,  $\text{Pe}\nabla \cdot \mathbf{p}$  and  $\text{Pe}\Delta\rho^2$  make the biggest contribution to the decrease of error. After that, the error stays at a more or less constant value, and then by an additional 7 term, the error decreases again. At the constant error around  $E \approx 0.4$ , the advection terms without  $\text{Pe}$ , such as  $\nabla \cdot (\rho\mathbf{p})$  and surface terms containing  $\Delta^2$  appear. Then, the error further decreases by  $\text{Pe}\Delta\rho^3$ . Finally, the error slightly decreases by the non-gradient term  $\mathcal{N}[\rho, \mathbf{p}] = 150.371\Delta|\mathbf{p}|^2$ , saturates at  $E \simeq 0.2832$ , and does not show a further decrease by adding other terms.

The essential term driving MIPS is  $\text{Pe}\nabla \cdot \mathbf{p}$ . Together with the estimation result of  $\mathbf{p} = b_2\nabla\rho^2$ , the term  $a_{14}\text{Pe}\nabla \cdot \mathbf{p}$  results in negative diffusion and destabilize the homogeneous state when  $a_{14} < 0$  and  $b_2 > 0$ . The negative diffusion is balanced with the positive diffusion term  $\text{Pe}\Delta\rho^2$ . This balance may be the reason for the main decrease in the error by  $\text{Pe}\nabla \cdot \mathbf{p}$  and  $\text{Pe}\Delta\rho^2$  for the density field. The coefficient  $a_{14}\text{Pe}$  corresponds to the negative sign of velocity of non-interacting active particles. In fact, our estimation shows  $a_{14} \approx -0.887$ , which is close to  $-1$  (see Fig. 7).

We perform the estimation for different time  $\tau_w$  and length  $k_{\max}$  scales. Figure 6(f) shows that the error of the estimation based on Eq. (6) is always large, whatever the time and length scales. This result also supports

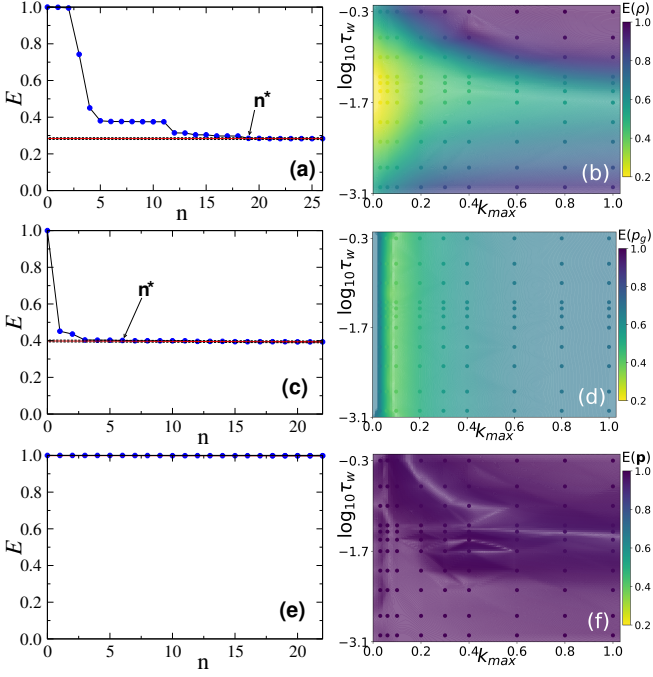


FIG. 6. (Color online) The three left plots show the error  $E$  vs  $n$  for (a) density, (c) polarity ( $\mathbf{p}$ , Eq. (14)), and (e) polarity ( $\partial \mathbf{p} / \partial t$ , Eq. (6)) in the Active Brownian particles at  $k_{\max} = 0.1$  and  $\tau_w = 0.02\tau$ . On the right, three plots depicted the corresponding variation of error  $E$  for density ( $\partial \rho / \partial t$ ) (b), polarity ( $\mathbf{p}$ , Eq. (14)) (d), and polarity ( $\partial \mathbf{p} / \partial t$ , Eq. (6)) (f) in the  $(k_{\max}, \tau_w)$  space, respectively.

the above-mentioned argument; the polarity density is not the hydrodynamic variable in this model. Instead, Fig. 6(d) shows smaller error at  $k_{\max} \approx 0.1$ . For the dynamic of density field, the minimum error is attained when  $\tau_w = 0.02\tau$  and  $k_{\max} = 0.03$ . Interestingly, the minimum error appears at the intermediate time scale. When the time scale is too long, the error starts to increase again.

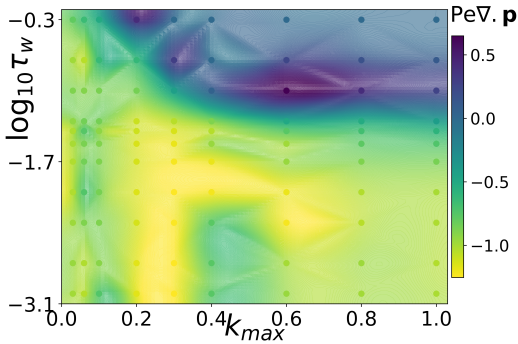


FIG. 7. (Color online) Plot of coefficients of dictionary terms  $\text{Pe} \nabla \cdot \mathbf{p}$  in  $(k_{\max}, \tau_w)$  space.

The dominant contribution to the small error for the density field of ABPs is  $\text{Pe} \nabla \cdot \mathbf{p}$ . When this term approaches -1, the error becomes smaller, as seen in Fig. 7.

At larger  $k_{\max}$  and larger  $\tau_w$ ,  $\text{Pe} \nabla \cdot \mathbf{p}$  deviates from -1. When  $\tau_w$  is smaller than  $10^{-2}\tau$ , the error increases. This is because the phase separation occurs at a longer time scale than local cluster formation, which is  $\approx \tau / \text{Pe}$ . We compare the time scale appearing in the estimation results and intrinsic time scales of ABPs in Sec. V A.

We classify the dictionary terms in the hydrodynamic equation of density field into bulk terms ( $\Delta \rho$ ,  $\Delta \rho^2$ ,  $\Delta \rho^3$ ,  $\text{Pe} \Delta \rho$ ,  $\text{Pe} \Delta \rho^2$ ,  $\text{Pe} \Delta \rho^3$ ), surface terms ( $\Delta^2 \rho$ ,  $\Delta^2 \rho^2$ ,  $\Delta^2 \rho^3$ ,  $\text{Pe} \Delta^2 \rho$ ,  $\text{Pe} \Delta^2 \rho^2$ ,  $\text{Pe} \Delta^2 \rho^3$ ), advection terms ( $\nabla \cdot \mathbf{p}$ ,  $\nabla \cdot (\rho \mathbf{p})$ ,  $\nabla \cdot (\rho^2 \mathbf{p})$ ,  $\text{Pe} \nabla \cdot \mathbf{p}$ ,  $\text{Pe} \nabla \cdot (\rho \mathbf{p})$ ,  $\text{Pe} \nabla \cdot (\rho^2 \mathbf{p})$ ), and non-gradient terms ( $\Delta |\mathbf{p}|^2$ ,  $\Delta (|\mathbf{p}|^2 |\mathbf{p}|)$ ,  $\nabla \cdot (\rho \nabla |\mathbf{p}|^2)$ ,  $\nabla \cdot (|\mathbf{p}|^2 \nabla \rho)$ ,  $\text{Pe} \Delta |\mathbf{p}|^2$ ,  $\text{Pe} \Delta (|\mathbf{p}|^2 |\mathbf{p}|)$ ,  $\text{Pe} \nabla \cdot (\rho \nabla |\mathbf{p}|^2)$ ,  $\text{Pe} \nabla \cdot (|\mathbf{p}|^2 \nabla \rho)$ ). Figure 8 shows the number of each term at different length and time scales. We can see that the advective terms appear in almost all scales, whereas the bulk and surface terms appear at larger length scales. Conversely, the non-gradient terms appear in smaller length scales.

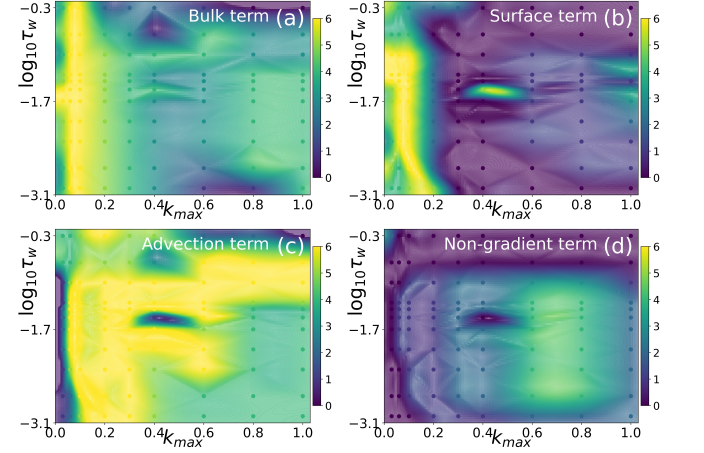


FIG. 8. (Color online) Plot of the estimated total number of bulk terms (a), the total number of surface terms (b), the total number of advection terms (c), and the total number of Non-gradient terms (d) in each point of the parameter  $(k_{\max}, \tau_w)$  space.

To analyze the estimation results further, we evaluate the effective free energy  $\mathcal{F}[\rho]$  from the estimated coefficients. We plug Eq. (13) into Eq. (12) to obtain the partial differential equation only for  $\rho$ . Then, we rewrite the hydrodynamic equation as[31]

$$\partial_t \rho = \Delta \frac{\delta \mathcal{F}}{\delta \rho} + \mathcal{N}[\rho] \quad (15)$$

where  $\mathcal{N}[\rho]$  is non-gradient terms, such as  $\Delta |\nabla \rho|^2$ . The effective free energy is expressed as

$$\mathcal{F}[\rho] = \int d\mathbf{r}^2 \left[ \tilde{f}_1(\rho(\mathbf{r}), \text{Pe}) + \tilde{f}_2(\rho(\mathbf{r}), \text{Pe}) |\nabla \rho(\mathbf{r})|^2 \right]. \quad (16)$$

Here,  $\tilde{f}_1, \tilde{f}_2$  are polynomials in  $\rho$  and up to second-order in  $\text{Pe}$ . They can be computed from  $f_1, f_2, f_3, g_1, g_2$  in



Eq. (13) into Eq. (12). We focus on the bulk part of the effective free energy  $\hat{f}_1$ , from which we can evaluate the coexistence line of the phase separation. In this analysis, we estimate the hydrodynamic equation for the density field by replacing  $\rho$  by  $\rho - \rho_0$  in the dictionary terms. We focus on the scales  $\tau_w = 0.02\tau$  and  $k_{\max} = 0.1$  when the error is lowest. In this case,  $n^* = 17$ . The estimated effective free energy reproduces two minima when  $Pe > 36$ . The minima of  $\hat{f}_1$  with respect to  $\rho$  is shown in Fig. 9 as a function of  $Pe$ . We also measure the histogram of local density in particle simulations of ABPs. The points in Fig. 9 are the peak densities of the histogram. At the quantitative level, the estimated coexistence curve deviates from the actual simulation results. Still, the estimated result qualitatively reproduces the  $Pe$  dependence of the phase separation. When we use fewer dictionary terms than the optimal  $n$ , the estimated effective free energy does not reproduce the coexistence of dense and dilute phases. On the other hand, including more terms does not improve the result. This analysis suggests that  $n^*$  is determined so that the estimated hydrodynamic equation can reproduce the  $Pe$  dependence of the phase separation. We should stress that our method does neither estimate the free energy directly nor assume its existence. We estimate dynamical equations of the continuum fields from the data of particle dynamics.

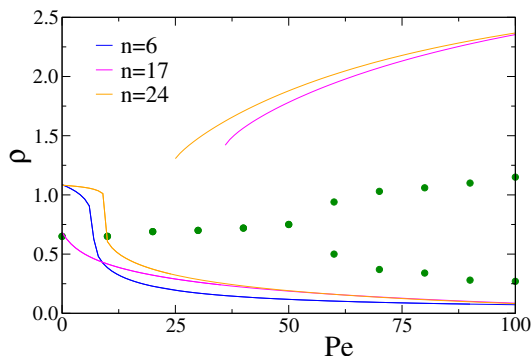


FIG. 9. (Color online) Plot of local density vs  $Pe$  for the system density  $\rho_0 = 0.65$ . At smaller values of  $Pe$ , the system is single-phase, and for increasing  $Pe$ , it phase-separates. Dotted points (green) are measured from the simulation of particle dynamics data. A solid line is drawn from the estimated effective free energy for different  $n = 6$  (blue), 17 (magenta), and 24 (orange).

## V. DISCUSSIONS AND CONCLUSION

To summarize, we propose a method to estimate hydrodynamic equations from data of microscopic particle dynamics. We transform data of the trajectory of individual particles into field data with the Gaussian kernel. Then, we apply spatial and temporal filters to the field data so that we obtain the coarse-grained data at different lengths and time scales. Using the method of

estimation of partial differential equations with encouraging sparsity, we can estimate the hydrodynamic equations corresponding to the coarse-grained data. As we stressed in the Introduction, the purpose of estimating the hydrodynamic equations is not to reproduce all the microscopic dynamics of particle simulations. It is instead to extract qualitative features hidden in complex microscopic dynamics. Our results suggest that the estimated hydrodynamic equations depend on the length and time scales we are looking at. Our method works both for the Vicsek model and ABP. In the following sections, we will discuss several issues to support our estimation results.

### A. time and length scales

In this section, we discuss the length and time scales in the Vicsek and ABP models. We compare them with the scales on which the estimation results depend. For the Vicsek model, the time scale unit is chosen by the time scale of alignment  $\tau = R^2/\kappa$ . The model has another time scale of collision  $\frac{R}{v_0} \sqrt{\frac{\pi}{\rho}}$ , which is  $\mathcal{O}(\tau)$  with our choice of parameters. The simulation results show that the time scale of global polarization is  $\tau_p \approx 200\tau$ . A small error is attained when  $\tau_w \simeq 10^2\tau$ . This is comparable with the time scale of global polarization. In fact, the relaxation time from the disordered state to the ordered state is  $40\tau - 200\tau$  depending on  $\eta$ . The major factor in decreasing the estimation error is advection terms, which play their roles after the polar-ordered state appears. The length scale of the polar band, which appears near the critical noise strength, is  $l \approx 50R$ .

The ABP model has a time scale of translational diffusion  $\tau = R^2/D$ , which we chose as a unit time scale. The time scale of rotational diffusion  $D_r^{-1} = \tau/3$  is comparable to  $\tau$ . The collision time scale is  $\frac{R}{v_0} \sqrt{\frac{\pi}{\rho}} \approx \tau/Pe$ . When the motility-induced phase separation occurs, first, many clusters appear at the time scale  $\tau_{cl}$  and then each cluster grows and shows coarsening with the time scale  $\tau_{gr}$  [27]. During the coarsening process, the fraction of particles in the gas phase does not change. The time scale  $\tau_{cl}$  is dominated by the collision time scale. With our choice of the system size,  $\tau_{gr} \approx 40\tau$ . Our results of estimation suggest that its error is small when  $\tau_w \geq 10^{-2}\tau$ , which is comparable to  $\tau_{cl}$  for large  $Pe$ . This is consistent with the fact that the hydrodynamic equation describes phase separation.

### B. generalizability

To check whether our estimated hydrodynamic equations are applicable to unseen data, we prepare independent data of microscopic particle simulations and perform a test using the estimated parameters. We coarse-grain

these new data and compute the error using the hydrodynamic equations with estimated coefficients for each  $n$  (see Fig. 2(b) and 6(a)). We perform the test at least 4 times and measure the error at  $n^*$  obtained for the training data. The results are  $E_{\text{test}} = 0.3460 \pm 0.0431$  for the polarity field of the Vicsek model with  $\tau_w = 40\tau$  and  $k_{\text{max}} = 0.1$ , and  $E_{\text{test}} = 0.2868 \pm 0.0026$  for the density field of the ABP with  $\tau_w = 0.02\tau$  and  $k_{\text{max}} = 0.1$ . These errors are comparable with those during training. The results demonstrate the generalizability of our estimated hydrodynamic equation.

### C. sparsity

When the hydrodynamic equations are estimated using sparse regression, there is always an issue of choosing the optimal number of terms included in the equations. In this section, we discuss the dependence of the error on the number of nonzero coefficients, which provides information on relevant physical properties in the hydrodynamic description. Figure 10 shows  $E(n)$  normalized by its smallest value  $E_0 = E(M)$  both in the Vicsek and ABP models. We show the results with different  $\tau_w$  but  $k_{\text{max}} = 0.1$  fixed. When normalized, all the results show the same trend. We may see that the error decreases in multiple steps.

For the Vicsek model, the error decreases in two steps at  $n_1^*$  and  $n_2^*$  (Fig. 10(a)). The large part of the error decrease arises from  $n_1^* = 4$  terms, which are 4 advection terms,  $\nabla\rho, (\mathbf{p} \cdot \nabla)\mathbf{p}, (\nabla \cdot \mathbf{p})\mathbf{p}, \nabla|\mathbf{p}|^2$ , discussed in Sec. III. The additional small decrease of the error occurs up to  $n_2^* = 8$ . The additional 4 terms are bulk terms, which are  $\mathbf{p}$  and  $|\mathbf{p}|^2\mathbf{p}$  with their coefficients are dependent on  $\rho$  and  $\eta$ . In contrast with the advection terms, these estimated bulk terms differ for different  $\tau_w$ . This result implies that the hydrodynamic description is dominated by the advection terms, whereas the bulk terms play the role of correction.

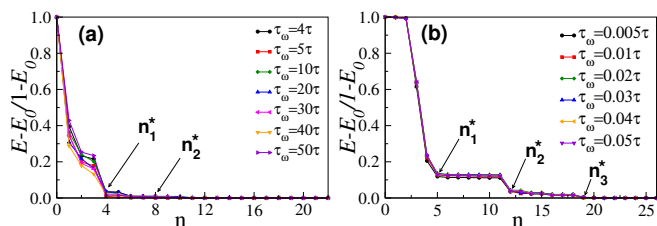


FIG. 10. (Color online) The plot of normalized error,  $(E - E_0)/(1 - E_0)$  vs the number of estimated terms  $n$  for (a) Vicsek Model and (b) Active Brownian particles. We choose  $k_{\text{max}} = 0.1$  for different time windows  $\tau_w$ .

For the ABP model, we found the three steps,  $n_1^*$ ,  $n_2^*$ , and  $n_3^*$  (Fig. 10(b)). After normalization, the error decreases in the same way for different  $\tau_w$ . The first drop of the error includes  $\text{Pe}\nabla \cdot \mathbf{p}$ ,  $\Delta\rho$ ,  $\Delta\rho^2$ ,  $\text{Pe}\Delta\rho^2$  and  $\text{Pe}\nabla \cdot (\rho\mathbf{p})$  terms. Those terms are independent of the

choice of  $\tau_w$ . Between  $n_1^*$  and  $n_2^*$ , 7 terms discussed in Sec. IV appear. Again, these terms are independent of the choice of  $\tau_w$ . On the other hand, the estimated terms between  $n_2^*$  and  $n_3^*$  are different for different  $\tau_w$ .

### D. suitable data to estimate hydrodynamic equations

During the estimation of the number of relevant terms, we eliminate dictionary terms one by one (see Fig. 1). The error decreases in multiple steps. In the first step, only the robust terms are estimated, whereas in the second step, less relevant terms are estimated. Those less relevant terms still decrease the error. This is in contrast with totally irrelevant terms, which does not decrease the error at all.

Here, we discuss whether bulk terms can be estimated or not, which is dependent on the way of preparing data. In short, information on transient dynamics is necessary to estimate the bulk terms; that is, the data should contain information on unstable states. When the data is dominated by the steady states, only the hydrodynamic terms are estimated. For example, in the Vicsek model, the polarity of particles is aligned and fluctuates around the steady state. In this case, only the advection terms are estimated. On the other hand, when the data contains the transient dynamics from disordered to ordered states and vice versa, the bulk terms may appear in the estimation. To see this, we perform the estimation using the data containing only transient dynamics. We perform the simulations of the Vicsek model at the time window of  $t \in [0, 400\tau]$  starting from a random initial condition. The maximum time is chosen so that the system does not reach a steady polar-ordered state. Collecting the data with 20 different noise strengths  $\eta = [0.100, 0.125, 0.150, 0.175, 0.200, 0.225, 0.250, 0.275, 0.300, 0.325, 0.350, 0.375, 0.400, 0.425, 0.450, 0.475, 0.500, 0.550, 0.600, 0.650]$ , we perform the estimation of hydrodynamic equations. From the estimated coefficients, we compute the estimated values of  $|\mathbf{p}| = \sqrt{-\alpha/\beta}$  at the steady state. The estimated  $|\mathbf{p}|$  as a function of local density  $\rho$  and the noise amplitude  $\eta$  is shown in Fig. 11. We perform independent simulations of the Vicsek model under the different mean density  $\rho_0$  and evaluate the critical value of noise amplitude for each  $\rho_0$  (points in Fig. 11). Although quantitatively, the estimated result does not match the simulations, the estimated (mean-field) transition line shows the correct dependence on local density and noise. This result indicates that to estimate the bulk terms precisely, the majority of the data should cover information on transient dynamics.

### ACKNOWLEDGMENTS

The authors acknowledge the support from the JSPS KAKENHI Grant number JP20K03874, 24H02203, and

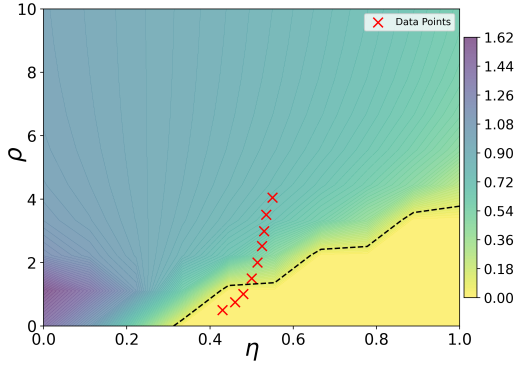


FIG. 11. (Color online) Phase diagram showing the transition from the ordered to disordered state in the  $(\rho, \eta)$  space, evaluated from  $\alpha$  and  $\beta$  using the estimated coefficients. The black dotted line indicates the phase boundary evaluated by  $|\mathbf{p}| = 0.1$ . The color bar on the right represents the magnitude of the polarity  $|\mathbf{p}|$ . The points shown by the crosses indicate  $\eta$  at the phase transition for different values of  $\rho_0$  in simulations.

JP24K00591 to N.Y. This work is supported also by the JST FOREST Program Grant Number JPMJFR2140 to N.Y.

## Appendix A: Appendixes

### 1. dictionary terms

$$\begin{aligned}
C_l = & \left( \nabla \cdot \mathbf{p}, \Delta \rho, \nabla \cdot (\rho \mathbf{p}), \Delta \rho^2, \Delta |\mathbf{p}|^2, \nabla \cdot (\rho^2 \mathbf{p}), \Delta \rho^3, \right. \\
& \nabla \cdot (|\mathbf{p}|^2 \mathbf{p}), \nabla \cdot (\rho \nabla |\mathbf{p}|^2), \nabla \cdot (|\mathbf{p}|^2 \nabla \rho), \Delta^2 \rho, \Delta^2 \rho^2, \\
& \Delta^2 \rho^3, \alpha \nabla \cdot \mathbf{p}, \alpha \Delta \rho, \alpha \nabla \cdot (\rho \mathbf{p}), \alpha \Delta \rho^2, \alpha \Delta |\mathbf{p}|^2, \\
& \alpha \nabla \cdot (\rho^2 \mathbf{p}), \alpha \Delta \rho^3, \alpha \nabla \cdot (|\mathbf{p}|^2 \mathbf{p}), \alpha \nabla \cdot (\rho \nabla |\mathbf{p}|^2), \\
& \left. \alpha \nabla \cdot (|\mathbf{p}|^2 \nabla \rho), \alpha \Delta^2 \rho, \alpha \Delta^2 \rho^2, \alpha \Delta^2 \rho^3 \right) \quad (\text{A1})
\end{aligned}$$

$$\begin{aligned}
D_l = & \left( \mathbf{p}, \rho \mathbf{p}, \rho^2 \mathbf{p}, |\mathbf{p}|^2 \mathbf{p}, \nabla \rho, (\mathbf{p} \cdot \nabla) \mathbf{p}, \nabla (\nabla \cdot \mathbf{p}), \Delta \mathbf{p}, \right. \\
& \nabla |\mathbf{p}|^2, (\nabla \cdot \mathbf{p}) \mathbf{p}, \Delta^2 \mathbf{p}, \alpha \mathbf{p}, \alpha \rho \mathbf{p}, \alpha \rho^2 \mathbf{p}, \alpha |\mathbf{p}|^2 \mathbf{p}, \alpha \nabla \rho, \\
& \alpha (\mathbf{p} \cdot \nabla) \mathbf{p}, \alpha \nabla (\nabla \cdot \mathbf{p}), \alpha \Delta \mathbf{p}, \alpha \nabla |\mathbf{p}|^2, \alpha (\nabla \cdot \mathbf{p}) \mathbf{p}, \\
& \left. \alpha \Delta^2 \mathbf{p} \right), \quad (\text{A2})
\end{aligned}$$

$$\begin{aligned}
\tilde{D}_l = & \left( \nabla \rho, \nabla \rho^2, \nabla \rho^3, \nabla (\Delta \rho), \nabla (\Delta \rho^2), \nabla (\Delta \rho^3), \right. \\
& \nabla |\nabla \rho|^2, (\nabla \rho) (\Delta \rho), \nabla \rho |\nabla \rho|^2, \rho (\nabla \rho) (\Delta \rho), \rho \nabla |\nabla \rho|^2, \\
& \text{Pe} \nabla \rho, \text{Pe} \nabla \rho^2, \text{Pe} \nabla \rho^3, \text{Pe} \nabla (\Delta \rho), \text{Pe} \nabla (\Delta \rho^2), \\
& \text{Pe} \nabla (\Delta \rho^3), \text{Pe} \nabla |\nabla \rho|^2, \text{Pe} (\nabla \rho) (\Delta \rho), \text{Pe} \nabla \rho |\nabla \rho|^2, \\
& \left. \text{Pe} \rho (\nabla \rho) (\Delta \rho), \text{Pe} \rho \nabla |\nabla \rho|^2 \right), \quad (\text{A3})
\end{aligned}$$

### 2. coefficients in Eqs.(12) and (13)

$$\begin{aligned}
f_1 = & -0.887 \text{Pe} - 0.492 \rho \text{Pe} + 0.370 \rho^2 \text{Pe} \\
& + 14.538 - 27.455 \rho + 13.692 \rho^2 \quad (\text{A4})
\end{aligned}$$

$$\begin{aligned}
f_2 = & 794.008 - 998.452 + 430.677 \\
& - 3.359 \text{Pe} + 2.235 \text{Pe} + 0.226 \text{Pe} \quad (\text{A5})
\end{aligned}$$

$$\begin{aligned}
f_3 = & 22969.929 - 20796.103 + 5533.872 \\
& - 184.109 \text{Pe} + 152.673 \text{Pe} - 34.304 \text{Pe} \quad (\text{A6})
\end{aligned}$$

$$g_1 = -10.422 + 7.784 + 0.0049 \text{Pe} - 0.0029 \text{Pe} \quad (\text{A7})$$

$$g_2 = -454.836 + 275.210 \quad (\text{A8})$$

[1] P. C. Hohenberg and B. I. Halperin, Theory of dynamic critical phenomena, *Rev. Mod. Phys.* **49**, 435 (1977).  
[2] M. C. Marchetti, J. F. Joanny, S. Ramaswamy, T. B. Liverpool, J. Prost, M. Rao, and R. A. Simha, Hydrodynamics of soft active matter, *Rev. Mod. Phys.* **85**, 1143 (2013).  
[3] A. Onuki, *Phase Transition Dynamics* (Cambridge University Press, 2002).  
[4] T. Vicsek, A. Czirók, E. Ben-Jacob, I. Cohen, and O. Shochet, Novel type of phase transition in a system of self-driven particles, *Phys. Rev. Lett.* **75**, 1226 (1995).  
[5] J. Toner and Y. Tu, Long-range order in a two-dimensional dynamical  $xy$  model: How birds fly together, *Phys. Rev. Lett.* **75**, 4326 (1995).  
[6] J. Toner, Reanalysis of the hydrodynamic theory of fluid,

polar-ordered flocks, *Phys. Rev. E* **86**, 031918 (2012).  
[7] Y. Fily and M. C. Marchetti, Athermal phase separation of self-propelled particles with no alignment, *Phys. Rev. Lett.* **108**, 235702 (2012).  
[8] M. E. Cates and J. Tailleur, Motility-induced phase separation, *Annu. Rev. Condens. Matter Phys.* **6**, 219 (2015).  
[9] Y. Fily, S. Henkes, and M. C. Marchetti, Freezing and phase separation of self-propelled disks, *Soft Matter* **10**, 2132 (2014).  
[10] E. Bertin, M. Droz, and G. Grégoire, Hydrodynamic equations for self-propelled particles: microscopic derivation and stability analysis, *Journal of Physics A: Mathematical and Theoretical* **42**, 445001 (2009).  
[11] T. Ihle, Kinetic theory of flocking: Derivation of hydrodynamic equations, *Phys. Rev. E* **83**, 030901 (2011).

- [12] H. Chaté, Dry aligning dilute active matter, *Annual Review of Condensed Matter Physics* **11**, 189 (2020).
- [13] T. Speck, J. Bialké, A. M. Menzel, and H. Löwen, Effective cahn-hilliard equation for the phase separation of active brownian particles, *Phys. Rev. Lett.* **112**, 218304 (2014).
- [14] I. S. Aranson and L. S. Tsimring, Pattern formation of microtubules and motors: Inelastic interaction of polar rods, *Physical Review E (Statistical, Nonlinear, and Soft Matter Physics)* **71**, 050901 (2005).
- [15] T. B. Liverpool and M. C. Marchetti, Instabilities of isotropic solutions of active polar filaments, *Phys. Rev. Lett.* **90**, 138102 (2003).
- [16] K. Kruse and F. Jülicher, Dynamics and mechanics of motor-filament systems, *The European Physical Journal E-Soft Matter* **20**, 459 (2006).
- [17] R. Suzuki, C. A. Weber, E. Frey, and A. R. Bausch, Polar pattern formation in driven filament systems requires non-binary particle collisions, *Nat Phys* **11**, 839 (2015).
- [18] S. Hijazi, M. Freitag, and N. Landwehr, Pod-galerkin reduced order models and physics-informed neural networks for solving inverse problems for the navier–stokes equations, *Adv. Model. and Simul. in Eng. Sci.* **10**, 5 (2023).
- [19] S. L. Brunton, J. L. Proctor, and J. N. Kutz, Discovering governing equations from data by sparse identification of nonlinear dynamical systems, *Proceedings of the National Academy of Sciences* **113**, 3932 (2016).
- [20] S. H. Rudy, S. L. Brunton, J. L. Proctor, and J. N. Kutz, Data-driven discovery of partial differential equations, *Science Advances* **3**, e1602614 (2017).
- [21] N. Yoshinaga and S. Tokuda, Bayesian modeling of pattern formation from one snapshot of pattern, *Phys. Rev. E* **106**, 065301 (2022).
- [22] Y. Gao and N. Yoshinaga, Inverse problems of inhomogeneous fracture toughness using phase-field models, *Physica D: Nonlinear Phenomena* **448**, 133734 (2023).
- [23] C. Joshi, S. Ray, L. M. Lemma, M. Varghese, G. Sharp, Z. Dogic, A. Baskaran, and M. F. Hagan, Data-driven discovery of active nematic hydrodynamics, *Phys. Rev. Lett.* **129**, 258001 (2022).
- [24] R. Supekar, B. Song, A. Hastewell, G. P. T. Choi, A. Mietke, and J. Dunkel, Learning hydrodynamic equations for active matter from particle simulations and experiments, *Proceedings of the National Academy of Sciences* **120**, e2206994120 (2023).
- [25] S. Maddu, Q. Vagne, and I. F. Sbalzarini, Learning deterministic hydrodynamic equations from stochastic active particle dynamics, arXiv:2201.08623 (2022).
- [26] R. Kürsten and T. Ihle, Dry active matter exhibits a self-organized cross sea phase, *Phys. Rev. Lett.* **125**, 188003 (2020).
- [27] G. S. Redner, M. F. Hagan, and A. Baskaran, Structure and dynamics of a phase-separating active colloidal fluid, *Phys. Rev. Lett.* **110**, 055701 (2013).
- [28] Y. Zhao, T. Ihle, Z. Han, C. Huepe, and P. Romanczuk, Phases and homogeneous ordered states in alignment-based self-propelled particle models, *Phys. Rev. E* **104**, 044605 (2021).
- [29] T. Hastie, R. Tibshirani, and J. Friedman, *The elements of statistical learning: data mining, inference, and prediction* (Springer, 2017).
- [30] The term  $\nabla\rho$  is often called a pressure term. However, we call it an advection term because it arises from the advective part of the Boltzmann equation.
- [31] E. Tjhung, C. Nardini, and M. E. Cates, Cluster phases and bubbly phase separation in active fluids: Reversal of the ostwald process, *Phys. Rev. X* **8**, 031080 (2018).